a reprint from Applied Optics

Signal processing and calibration of continuous-wave focused CO_2 Doppler lidars for atmospheric backscatter measurement

Jeffry Rothermel, Diana M. Chambers, Maurice A. Jarzembski, Vandana Srivastava, David A. Bowdle, and William D. Jones

Two continuous-wave (CW) focused CO_2 Doppler lidars (9.1 and 10.6 μm) were developed for airborne *in situ* aerosol backscatter measurements. The complex path of reliably calibrating these systems, with different signal processors, for accurate derivation of atmospheric backscatter coefficients is documented. Lidar calibration for absolute backscatter measurement for both lidars is based on range response over the lidar sample volume, not solely at focus. Both lidars were calibrated with a new technique using well-characterized aerosols as radiometric standard targets and related to conventional hard-target calibration. A digital signal processor (DSP), a surface acoustic wave spectrum analyzer, and manually tuned spectrum analyzer signal analyzers were used. The DSP signals were analyzed with an innovative method of correcting for systematic noise fluctuation; the noise statistics exhibit the chi-square distribution predicted by theory. System parametric studies and detailed calibration improved the accuracy of conversion from the measured signal-to-noise ratio to absolute backscatter. The minimum backscatter sensitivity is $\sim 3 \times 10^{-12}$ m^{-1} sr^{-1} at 9.1 μm and $\sim 9 \times 10^{-12}$ m^{-1} sr^{-1} at 10.6 μm. Sample measurements are shown for a flight over the remote Pacific Ocean in 1990 as part of the NASA Global Backscatter Experiment (GLOBE) survey missions, the first time to our knowledge that 9.1–10.6-μm lidar intercomparisons were made. Measurements at 9.1 μm, a potential wavelength for space-based lidar remote-sensing applications, are to our knowledge the first based on the rare isotope $^{12}C\,^{18}O_2$ gas.

1. Introduction

Airborne continuous-wave (CW) lidars provide an effective means of performing high-spatial-resolution sampling of aerosol backscatter in the troposphere and the lower stratosphere.[1–4] A CW 10.6-μm Doppler lidar was developed at the Marshall Space Flight Center (MSFC) shortly after 1979,[5–7] and it has been used in both ground and airborne experiments.[8–9] In response to a growing interest in detailed characterization of tropospheric backscatter at infrared wavelengths, a Doppler lidar was developed in 1988–1989, based on an improved optical design of the 10.6-μm lidar and operating at the $^{12}C\,^{18}O_2$ rare isotopic line of 9.1 μm. This wavelength was selected to match that of a prospective space-based Doppler lidar.[10] Moreover, a 9.1–10.6-μm lidar combination provides information on the wavelength dependence of atmospheric aerosol backscatter. Both lidars were operated during the NASA-sponsored Global Backscatter Experiment (GLOBE) flight survey missions, intensive airborne measurement programs conducted in 1989 (GLOBE I) and 1990 (GLOBE II) to obtain aerosol physical, chemical, and optical measurements over the remote Pacific Ocean.[11]

Results from the GLOBE program guide instrument design and performance studies of prospective satellite Doppler lidars for tropospheric wind profiling. A major GLOBE objective was to characterize low-backscatter conditions in the comparatively clean

J. Rothermel and M. A. Jarzembski are with the Earth System Science Division, Global Hydrology and Climate Center, NASA Marshall Space Flight Center, 977 Explorer Boulevard, Huntsville, Alabama 35806. D. M. Chambers is with Micro Craft, Inc., 620 Discovery Drive, Huntsville, Alabama 35806. V. Srivastava and D. A. Bowdle are with the Institute for Global Change Research and Education, Universities Space Research Association, Global Hydrology and Climate Center, 911 Explorer Boulevard, Huntsville, Alabama 35895. W. D. Jones is with the Optical and Radio Frequency Division, NASA Marshall Space Flight Center, Huntsville, Alabama 35812.

Received 13 January 1995; revised manuscript received 29 November 1995.

0003-6935/96/122083-13$06.00/0

middle and upper troposphere, primarily over the remote Pacific Ocean, where backscattered signals may approach the limit of detection for such an instrument and where new wind measurements could have a major scientific impact.[10] Therefore an extensive calibration of the MSFC lidar systems was performed, and the combined performance of lidar instruments, data systems, and signal-processing algorithms was characterized. This process resulted in improved accuracy of the measured aerosol backscatter. In this paper, a description of the MSFC CW Doppler lidars (Section 2), data systems (Section 3), signal-processing algorithms for estimation of signal-to-noise ratio (SNR) (Section 4), and operating characteristics (Section 5) is given. The lidar calibration procedure and conversion of SNR to backscatter are described in Section 6. Examples of aerosol backscatter estimates from GLOBE II are given in Section 7. Finally, conclusions on overall performance and measurement sensitivity are given in Section 8.

2. Lidar Systems

Figure 1 is a schematic of the optical layout of the 9.1-μm CW Doppler lidar system. The MSFC 10.6-μm CW lidar has been described previously.[8] Both lidars use a monostatic optical configuration, with coherent (homodyne) Doppler detection. Slight differences in optical design and component specifications are noted below. The MSFC 9.1-μm lidar system is, to our knowledge, the first to be designed and operated specifically at this rare isotopic CO_2 wavelength.

The 9.1-μm lidar is based on a Line Lite[12] 5-W water-cooled, sealed gas laser, filled with a gas mixture of $^{12}C\ ^{18}O_2$, N_2, He, and Xe and operating at the fundamental mode TEM_{00}. The laser is grating tunable over the wavelength range 9.0–9.5 μm, with

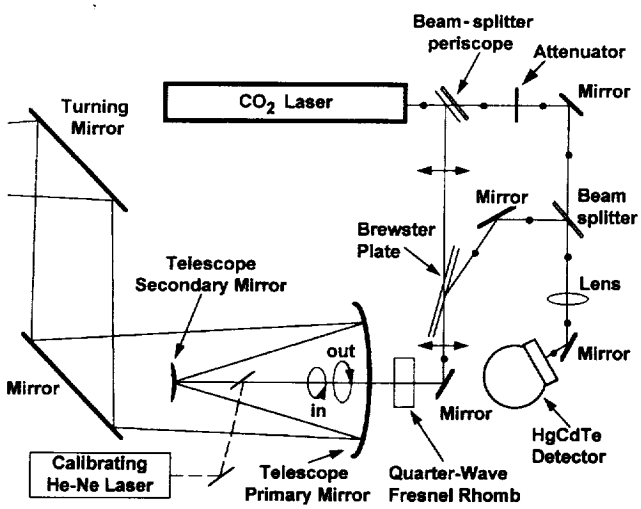

Fig. 1. Schematic of the NASA Marshall Space Flight Center (MSFC) 9.1-μm CW focused coherent Doppler lidar. The dots and two-headed arrows along optical path indicate perpendicular and parallel polarization, respectively. The 10.6-μm CW lidar has a similar configuration; differences are noted in the text.

optical components optimized for 9.1 μm. Within the lidar optics, the perpendicular polarized laser beam strikes a beam splitter, at which ~98% of the incident radiation is reflected to the atmosphere and the remaining ~2% is transmitted to serve as the reference local oscillator (LO) for coherent detection. The LO is passed through an attenuator to adjust beam intensity for optimum detection before the beam is focused on the detector. By the use of a periscope, the transmitted perpendicular polarized beam is transformed into a parallel polarized beam. After transmission through a germanium Brewster plate, the beam is converted to circular polarization by a quarter-wave Fresnel rhomb. The beam is then expanded by a convex secondary mirror to a 0.10-m-diameter off-axis parabolic primary mirror, from which the beam is reflected to two flat mirrors (the second is used for single-axis beam steering) before being transmitted through a 0.18-m-diameter germanium window into the atmosphere. The range to focus is varied by adjustment of the axial position of the secondary mirror with respect to the primary mirror. For the GLOBE missions, the beam was focused at ~10 m (GLOBE I) and ~50 m (GLOBE II) from the aircraft into the undisturbed atmosphere beyond the slipstream of the DC-8. For GLOBE II the longer focal distance effectively increased the sample volume, with the expectation that aerosol sampling statistics in low aerosol concentration conditions would be improved.

The circular polarization of the incident beam is reversed upon backscattering of the beam by atmospheric aerosols. The backscattered radiation then retraces the path of the outgoing beam through the telescope and is converted to perpendicular polarization by the Fresnel rhomb, reflected at the Brewster plate, and directed to the recombining beam splitter, where it is mixed with the reference LO beam. The combined beams are then focused onto a liquid-nitrogen-cooled HgCdTe photodiode detector. The output signal from the detector oscillates at the beat frequency of the reference and the backscattered beams. The beat frequency arises from the Doppler shift introduced in the backscattered beam by aerosol motion along the line of sight. The time-varying detector output undergoes two-stage amplification (~54.3 dB) before being sent to the signal-processing systems.

For optimum coherent detection, the backscattered and the reference LO beams must be accurately coaligned. All lidar optics are secured to a small optical table (0.4 m × 1.1 m), which is attached to a low-profile support structure with shock-absorbing mounts to minimize misalignment from disturbances during flights or laboratory operation. Occasional realignment was performed with a coaligned He–Ne laser beam.

The design of the 10.6-μm lidar is nearly identical to that of the 9.1-μm lidar. Primary differences between the two systems lie in individual component specifications. A Line Lite 12-W water-cooled, sealed

gas laser with a gas mixture of $^{12}C\ ^{16}O_2$, N_2, He, and Xe is used; the laser uses a fixed back mirror, with no wavelength-tuning capability. A quarter-wave plate is used instead of the quarter-wave Fresnel rhomb, and the 10.6-μm lidar primary mirror is ~25% larger in diameter.

3. Data Systems

During GLOBE I, a Raytheon surface acoustic wave (SAW) spectrum analyzer (SA) and a manually tuned Hewlett Packard SA were used. Several performance limitations and anomalies were observed. Therefore, before GLOBE II these analog signal devices were supplemented by a third signal analyzer based on relatively recent advances in digital signal-processing (DSP) technology. The SAW and SA outputs are directly proportional to voltage, whereas the DSP output is proportional to power. In the following discussion, S_V and S_P refer to signal spectra proportional to voltage and power, respectively, and N_V and N_P refer to noise spectra proportional to voltage and power, respectively. Table 1 summarizes the primary characteristics of each signal analyzer. Each lidar has a dedicated DSP signal-processing system, whereas the SAW and the SA must be manually switched between lidars. Detailed laboratory studies have been conducted to characterize independently the performance of these three data systems. Comparisons of simultaneous lidar measurements with these three systems provide an internal cross check on signal estimation.

A. Digital Signal-Processing System

This system consists of an 80386SX 16-MHz industry standard architecture personal computer (PC) with peripheral boards added to fulfill the requirements for a complete data collection and analysis system. Signal processing is accomplished by a DSP board based on an American Telephone and Telegraph WE DSP32C chip; this board is combined with a Transient Capture Board (TCB) in a master–slave relationship through a dedicated bus. The PC controls system operation, performs data analysis and display, and archives lidar data and auxiliary data to an external write-once-read-many optical disk. Lidar data are transferred from the DSP board to the PC through the standard bus.

The output signal from the lidar is sent directly to the TCB. There it is amplified and low-pass filtered below 6.5 MHz before being digitized at 13.3 MHz with 8-bit resolution. The DSP reads data from the TCB in sets of 128 samples, applies a Hamming window, and generates a power spectrum by the use of a fast Fourier transform. The resulting spectrum has ~0.1-MHz resolution in each of its 64 channels, yielding a velocity resolution of ~0.5 ms^{-1} (λ = 10.6 μm). The single-channel bandwidth of the DSP as determined with narrow-band input signals is ~0.143 MHz (full width at half-maximum). Successive power spectra are integrated on a channel-by-channel basis to improve overall system sensitivity. The integration period is terminated by the PC at 1-s intervals, which allows 2295 spectra to be accumulated. The integrated spectrum is transferred to the PC for analysis, display, and archival while the TCB and the DSP continue to collect lidar data.

Table 1. Significant Data System Features

Parameter	Spectrum Analyzer (SA)	Surface Acoustic Wave Spectrum Analyzer (SAW)	Digital Signal Processor (DSP)
GLOBE Survey Mission	I, II	I, II	II
Output	signal, noise amplitude	amplitude spectrum	power spectrum
Frequency range (MHz)	0–10	0–6.0	0–6.5
No. of Channels	1	64	64
Channel bandwidth (MHz, FWHM)	0.36	0.181	0.143
Channel resolution (MHz)	0.36	0.104	0.102
Time to acquire a single spectrum (s)	–	5.8×10^{-6}	1.0×10^{-5}
No. of integrations (s^{-1})	manual	65,536	2295
Storage medium	operator logs	magnetic tape	optical disk

B. Surface Acoustic Wave Spectrum Analyzer

The surface acoustic wave (SAW) spectrum analyzer (SA) uses a SAW delay line technique, an analog-to-digital converter, and a video spectrum integrator. The performance of the spectrum analyzer is optimum for input frequencies between 0 and 6 MHz; beyond this range, resolution degrades and sensitivity decreases sharply. The response of the SAW to a narrow-band input signal is ~0.181 MHz (full width at half-maximum). The dynamic range is ~35 dB for fixed gain; manual gain adjustments provide an additional 30 dB of range. The SA output is digitized at 8-bit resolution and sent to the integrator, where it is amplified, envelope detected, and digitized at 0.104 MHz per filter, or channel. Batch integration is performed by summation of corresponding channels from successive spectra into a 20-bit multichannel accumulator. Accumulator contents, up to a maximum of 4096 integrated spectra, are periodically transferred to output memory and stored on cassette magnetic tape. Further integration to 1 s is performed during postflight data processing, for a total of 65,536 independent spectra in each data block. The SAW output is directed serially to a PC for in-flight processing, display, and archival while the SAW continues to collect and analyze data.

C. Manually Tuned Spectrum Analyzer

The manually tuned spectrum analyzer (SA) consists of a single scanning filter with an input frequency responsivity of 0–10 MHz and a filter bandwidth of

~0.36 MHz. Periodic measurements of detector signal and noise are obtained by manual tuning of the SA center frequency to alternately include and exclude the signal, respectively. The resulting measurements (in volts rms) are manually time tagged and logged. Although the SA has the advantage of being straightforward to use, it has the disadvantage of low throughput and fixed bandwidth. Thus it is used primarily for spot checks of the other data systems and for lidar calibration.

4. Signal-Processing Algorithm

Procedures for calculating SNR are generally similar for all three data systems and can be summarized as (a) initial estimation of signal peak location within the spectrum, (b) estimation of system noise applicable to the spectrum being analyzed, (c) refinement of signal peak location and signal width, (d) calculation of total signal power and total noise power contained in the return signal, (e) calculation of SNR, and (f) conversion of SNR to aerosol backscatter coefficient $\beta(\pi)$ (in inverse meters per steradian, m^{-1} sr^{-1}). Application to each data system, and differences in implementation among data systems, are described in the subsections below.

The initial estimate of signal peak location within the passband is obtained in the same manner for each data system. The Doppler-shifted frequency of the signal peak corresponds to the component of aircraft velocity along the lidar line of sight. Thus one may estimate the signal peak position by collecting true airspeed from the housekeeping data stream and combining it with a measurement of the angle between transmitted lidar beam and aircraft fuselage. The first-guess peak position is then used to establish a narrow search window in which the true peak is expected to be found. The largest uncertainty in this calculation is usually due to measured lidar beam angle. Aircraft maneuvers that introduce sideslip contribute additional uncertainty, due to an added, unknown component of motion along the line of sight. For moderate signal, these uncertainties do not significantly affect the signal retrieval process. However, for weak signals these uncertainties can influence the first guess of signal position, hence degrade the signal retrieval.

System noise spectra and variations are estimated by the use of different methods for the three data systems, which are described below. Signal location and width and baseline noise are determined automatically by algorithm for the SAW and the DSP. The signal peak position is refined by location of the channel within the search window with the maximum difference between signal amplitude and estimated noise in the absence of signal. For a strong to moderate signal, the exact peak position can be readily located. Problems arise for weak signals, especially where the signal straddles two adjacent channels in the SA. Signal width is represented by the number of contiguous channels surrounding the peak in which the difference between measured amplitude and estimated noise is greater than two standard deviations, 2σ, of the expected noise variation. The SA is handled differently because measurements are made manually in a single filter channel.

After estimation of total signal power and total noise power, calculation of SNR is similar for all systems. Total signal is the accumulation of signal plus noise contained in the signal width. SNR is obtained by subtraction of total noise power from total signal power and division by noise power, where noise in both cases applies to the signal window. Details for each data system are given below.

A. DSP System

Noise estimation is based on the mean spectral response when no signal is being returned to the lidar. A mean spectrum, $M(k)$, where k is the channel index, is calculated by means of averaging a statistically significant number of noise spectra over 0.5–12 min. The mean noise spectrum is used to correct individual backscatter signal spectra for short-term, systematic fluctuations in lidar system response. A noise fluctuation factor, G, is determined for each signal spectrum by comparison with the mean noise spectrum in a window of channels that do not contain signal. The comparison window contains 10 contiguous channels between the backscatter signal and the zero-frequency reference LO signal. G is calculated by minimization of the mean square error in channel amplitude between the two spectra,

$$e = \sum_{k=k_l}^{k_u} |S_p(k) - GM_p(k)|^2, \tag{1}$$

which yields

$$G = \frac{\sum_{k=k_l}^{k_u} S_p(k)M_p(k)}{\sum_{k_l}^{k_u} |M_p(k)|^2}, \tag{2}$$

where e is the sum-of-squares error, k_l and k_u are the lower and upper channels of the comparison window, respectively, and $S_p(k)$ is the signal strength (signal plus noise) in a channel. This method assumes that G is independent of frequency in the signal and mean noise spectra.

The SNR is calculated by

$$\mathrm{SNR_{DSP}} = \frac{\sum_{k=k_0}^{k_1} |S_p(k) - GM_p(k)|}{\sum_{k=k_0}^{k=k_1} GM_p(k) \Big/ n}, \tag{3}$$

subject to the criterion

$$S_p(k) - GM_p(k) > 2\sigma, \tag{4}$$

where k_0 and k_1 are the lower and upper channel limits of contiguous signal above threshold, respectively, and $n = k_1 - k_0$. Fluctuations in G are ostensibly due to fluctuations in LO power. These fluctuations affect both signal and noise and therefore effectively cancel out of Eq. (3).

B. SAW System

Signal is identified in the integrated SAW spectrum by the use of a technique described in detail in Ref. 13. Unlike the method for the DSP, estimation of noise is based on each signal spectrum. Establishment of a mean noise spectrum is problematic, as the SAW occasionally exhibits short-term variations in the mean noise distribution compared with the DSP (see Subsection 5.D.). Instead, noise is estimated by establishment of two windows of fixed size (10 channels, ~1.0 MHz), one on each side of the signal and adjacent to the signal window (see figure 4 of Ref. 13). A quadratic curve representing the general shape of the noise floor is fitted to the data within each noise window. A baseline or mean noise distribution is obtained by linear interpolation between the inner endpoints of each curve. The SNR is calculated by

$$\mathrm{SNR}_{\mathrm{SAW}} = C \frac{\sum_{k=k_0}^{k_1} [S_V^2(k) - N_V^2(k)]}{\left[\sum_{k=k_0}^{k_1} N_V^2(k)\right] \Big/ n}, \tag{5}$$

subject to the criterion

$$S_V^2(k) - N_V^2(k) > 2\sigma, \tag{6}$$

where σ is now the standard deviation about the quadratic fit in the noise windows, $S_V(k)$ is the kth signal channel of an integrated voltage spectrum (signal plus noise), $N_V(k)$ is baseline noise, and C is an instrument nonlinearity correction function defined in Section 5. Because SAW output is proportional to a voltage spectrum, SAW output is squared before signal integration and SNR estimation to preserve the proportionality between backscatter and the integrated SNR.[14,15]

C. SA System

SNR is calculated for the SA data system in a fundamentally different manner. Unlike the relatively broad, multichannel bandwidth of the DSP and SAW, which permits signal identification and SNR processing with autonomous algorithm techniques, the SA requires that one manually sweep a single narrow-band filter (~0.36 MHz) across a range of input frequencies while signal output S_V is maximized. Aerosol backscatter signal is Doppler shifted by ~3 MHz for typical airspeeds. All but exceptionally strong atmospheric signals (e.g., cloud returns) are contained within the SA bandwidth. The noise level is nearly constant for frequencies greater than ~1.5 MHz and exhibits negligible temporal variation; however, for lower airspeeds and frequencies less than ~1.5 MHz, the strong DC component of the reference LO signal substantially raises the noise level. Consequently, the noise level N_V in the absence of signal is estimated from the noise level in a frequency range ~2 MHz higher than the signal, where there is no contamination from atmospheric or DC signals. SNR proportional to power is then determined by

$$\mathrm{SNR}_{\mathrm{SA}} = \frac{S_V^2 - N_V^2}{N_V^2}. \tag{7}$$

5. Data System Performance

Comparisons among the three data systems have been conducted from signals generated in the laboratory and from GLOBE flight data. Results provide insight into data system performance, as described below.

A. DSP System

The performance of the DSP system may be easily traced to theory, because the hardware components develop the signal and noise digitally and the software algorithm calculates the frequency spectrum in power units. All components of the system were verified individually; then the system was tested as a unit to evaluate its linearity of response and its conformity to theoretical noise statistics. Methods of testing the data system as a unit are discussed here as well as diagnostics that were developed to accept or reject data collected during airborne experiments.

The linearity of the DSP system includes both the response of multiple channels to a constant input signal and the response of a single channel to a varying input signal. Response to a constant input signal was verified by generation of a narrow-bandwidth signal and scanning the center frequency across the passband. Special attention was given to the typical band of signal positions observed during GLOBE. The response in all channels was constant to within a few percent. Single-channel linearity was tested by combination of output from a noise generator and a signal generator equipped with a variable attenuator. Signal attenuation was varied in 2-dB increments over an ~46-dB range to duplicate the conditions encountered during GLOBE. Single-channel response varied linearly through the entire SNR range.

Noise statistics for the DSP were expected to conform to a chi-square distribution, a consequence of integrating spectra derived from zero-mean, complex Gaussian sampled voltages.[16] This distribution was confirmed by means of using the DSP to collect spectral data from the noise generator for several minutes and computing a mean noise spectrum, $M(k)$. A standard deviation, $\sigma(k)$, about the

mean was then calculated for each channel, and $\sigma(k)/M(k)$ was calculated and compared with the theoretical value for the given number of degrees of freedom for that data set. Initial comparisons indicated a ratio much larger than theory. However, when the standard deviation was calculated about a mean spectrum that had been adjusted for fluctuations in system response as described above $[GM(k)]$, the ratio $\sigma(k)/GM(k)$ for each channel matched the expected value $\sigma/\mu = 1/N^2 \cong 0.021$ to within a few percent for $N = 2295$ integrations. This relationship is used to derive the values of σ used in Eq. (4). Ratios differing from theory by more than 10–20% may indicate the influence of anomalies originating independently of the signal processor, such as electronic interference. These data are subjected to reprocessing (as described below) and, if necessary, are rejected from SNR calculations.

The noise fluctuation factor G is also used to indicate anomalous system performance. Ideally, $G \sim 1$, indicating no significant change in system operation. Variations from unity of greater than 10–20% may indicate significant changes in system behavior, requiring closer inspection and perhaps reprocessing of the data. For example, large G can indicate that the window used to calculate G has been contaminated by signal because of a poor first guess of signal location. As noted above, a poor first guess was usually the result of an unknown, and varying, component of motion along the line of sight, as caused by an aircraft turn, or because of unusually broad signals, as characterized by a strong return from a turbulent cloud. In most instances, one may recover questionable data by repositioning the comparison window $k_l, \ldots, k_u$, recalculating G, and recalculating SNR. If this procedure is unsuccessful, the data are excluded from processing. Additional diagnostics are discussed at the conclusion of this section.

B. SAW System

Evaluation of SAW performance followed the same procedure as for the DSP system. The SAW response is linear across the range 0–6 MHz for constant input signal level; above 6 MHz, the response degrades sharply.

Unlike SNR_{DSP}, which is directly proportional to signal power, SNR_{SAW} was found to vary nonlinearly over the range of input signal power. Because the DSP system exhibits the correct response, quantitative comparisons were made between the SAW and DSP. Signal from a frequency generator was combined with output from a random noise generator and split equally between the SAW and DSP. A comparison of SNR_{SAW} with SNR_{DSP} is shown in Fig. 2(a), in which bandwidth differences have been taken into account. SNR_{SAW} is overestimated for strong signals and underestimated for weak signals. The same trend is apparent in measurements from one of the GLOBE flights, as shown in a similar comparison in Fig. 2(b). With the field performance of the

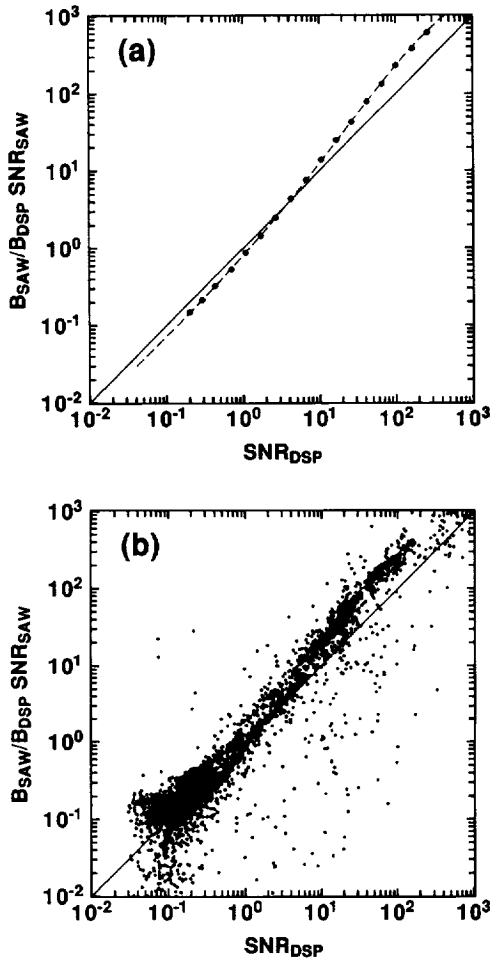

Fig. 2. Intercomparison measurements of SNR with DSP and SAW signal analyzers: (a) scatterplot of the laboratory study using combined output from signal and random noise generators and using stepped attenuation of the signal to simulate the range of the SNR from atmospheric targets (the dashed curve represents nonlinear correction function for SAW, as described in the text), (b) scatterplot of SNR_{DSP} and SNR_{SAW} for atmospheric measurements from GLOBE II, based on 11,500 (5-s) and 65,536 (1-s) integrations, respectively. Note the similarity in trends.

SAW thus reproduced in the laboratory, an empirical correction function for SNR_{SAW} was derived with the ratio between SNR_{DSP} and SNR_{SAW} estimates shown in Fig. 2(a) and given by

$$C = 0.953 - 0.249(\log \mathrm{SNR}_{SAW}) - 0.071(\log \mathrm{SNR}_{SAW})^2 + 0.028(\log \mathrm{SNR}_{SAW})^3, \quad (8)$$

where SNR_{SAW} in this instance refers to uncorrected signal-to-noise ratio. The nonlinear response of the SAW, which was manufactured in the 1970's, is attributed to degradation of the SAW electronics.

With exceptions resulting from occasional anomalies in the analog-to-digital converter, noise statistics for squared SAW output also conform to chi-square theory, $\sigma(k)/M(k) = N^{-1/2} \cong 0.004$ for $N = 65{,}536$ integrations. However, as noted above, the mean noise floor exhibits shorter-term variations com-

pared with the DSP, prohibiting routine application of the responsivity correction method used for DSP. Such variations would seriously interfere with SNR estimation for weak signals.

C. SA System

Laboratory studies similar to the above verified that the SA exhibits a linear response to constant input signal over the range 0–10 MHz. In comparison tests with narrow-band signals, SNR calculations from SA and DSP measurements are in excellent agreement. SA is the preferred data system for estimation of SNR during calibration because no elaborate signal processing is required in real time. The chief limitations of the SA are broad input bandwidth and low throughput; both contribute to poorer sensitivity to weak signals. For signals from rotating hard targets and typical aerosol signals encountered during GLOBE, which are broader than the output from the signal generator, SNR_{SA} is ~ 1.0 dB lower than SNR_{DSP}. This finding is consistent with the limited bandwidth of the SA, which under some conditions truncates the tails of a broad signal (Section 4).

D. Discussion

In evaluating backscatter measurements during GLOBE with the CW lidars, the primary issue has been accurate characterization of weak signals. This condition will present the severest test for satellite Doppler lidar that relies on aerosols in the relatively clean middle and upper troposphere[1–3] to measure some primary atmospheric variable, e.g., wind.[10] Two procedures have been developed to assess the validity of weak signals measured by the SAW and DSP signal analyzers; one is implemented during data collection, the other during postflight data processing. In the first procedure, the outgoing lidar beam is periodically blocked during weak scattering signal conditions, while integrated output spectra from the SAW and DSP are monitored. A prospective signal is determined to be valid if it vanishes and reappears as the outgoing beam is blocked and unblocked, respectively. If no effect is discerned, then the true atmospheric signal is below the lidar detection threshold. For GLOBE these observations were manually recorded and time tagged with the aircraft housekeeping data. These records were then used during postflight data processing to evaluate data quality under marginal signal conditions (planned improvements include automation of this procedure). In the second procedure, the difference between the Doppler velocity of the return signal and the component of aircraft velocity along the line of sight is calculated for each spectrum and analyzed as a function of SNR for each flight (see Section 3 of Ref. 17 and accompanying figures). In the absence of sharp aircraft turns, moderate turbulence, or other factors contributing an additional, unknown line-of-sight velocity component, speed difference values for valid signals are tightly distributed about zero regardless of signal strength. By contrast, noise peaks have speed differences that are randomly distributed over the signal search window and are clearly distinguishable from valid signals.[13,17] These false alarms, noise peaks incorrectly identified as signal, are flagged during postflight processing and excluded from final datasets.

6. Calibration

Measured SNR in a given lidar sample volume is converted to aerosol backscatter coefficient $\beta(\pi)$ (in m^{-1} sr^{-1}) by (equation 24 of Ref. 18, including a correction factor of 2 and regrouping terms):

$$\beta(\pi) = \mathrm{SNR}\,\frac{KB}{P_T}, \tag{9}$$

where P_T is the lidar transmitted power, B is the bandwidth of the data system, and K is a calibration factor. K includes total lidar system efficiency η and is given by

$$K = \left\{\left(\frac{\eta\lambda}{h\nu}\right)\left[\frac{\pi}{2} + \tan^{-1}\left(\frac{\pi R^2}{\lambda F}\right)\right]\right\}^{-1}, \tag{10}$$

where R is e^{-2} beam radius at the lidar primary telescope, F is focal distance, λ is wavelength, and $h\nu$ is photon energy. All parameters in Eqs. (9) and (10) can be measured directly except for η, which in this study represents the combined effect of optical, detector, and heterodyne efficiency, shot-noise correction, and unexplained losses. Thus the primary objective of the lidar calibration procedure is to determine η, including the effects of all system nonidealities. For given lidar operating conditions, this involves measurement of SNR from a calibration scattering target with known reflectance or backscatter properties. This section describes the steps in the GLOBE calibration procedure and explains the rationale for relating calibration results obtained under field conditions to more rigorous calibration with improved scattering targets subsequently performed in the laboratory. Careful attention is given to the derivation of transfer functions that account for differences in the scattering targets and measurement approaches that were used during and after GLOBE.

During GLOBE, a hard target (HT) with known reflectance properties (described below) was used as a field calibration standard. Typical HT's are composed of densely packed large particles bound to a plane disk, which differ greatly in scattering cross section from randomly dispersed atmospheric aerosols with smaller particles and lower concentration. HT's such as these give backscattered signals that can be many orders of magnitude greater than signals from aerosols.

The extreme magnitude of signals returned from the HT during calibrations requires temporary adjustment of the lidar and data processing equipment to avoid exceeding the dynamic range of ultrasensi-

tive receivers optimized for weak aerosol signals. Optical or electronic attenuation, or reduction in postdetector amplification as in the case of GLOBE field calibrations, must be introduced in the return signal path. The attenuation or reduced amplification must then be taken into account during data processing. This procedure has the potential to introduce additional uncertainties or biases to the calibration, hence to atmospheric backscatter measurements based on the calibration. Consequently the most desirable calibration target should exhibit a scattering cross section comparable to atmospheric aerosols both in spatial distribution and magnitude. This would permit lidar calibration with a signal measurement configuration and processing methodology identical to that used for atmospheric measurements.

These concerns led to development of a new calibration method to remove uncertainties associated with HT methods.[19] The new method is based on scattering from laboratory-generated aerosol particles with known size, complex index of refraction, and number concentration, which results in known backscatter. Details of the technique, including comparison with conventional HT methods, are described elsewhere.[19] The technique involves calibration with many particles in the lidar sample volume (volume mode, VM), similar to atmospheric aerosols. Although the new VM method permits calibration under more realistic conditions, currently the method requires controlled laboratory conditions that are difficult to implement in the field. In contrast the HT method, used during GLOBE, is simpler to implement in the field because of its ease of transport and maneuverability. Thus a multistep procedure was devised to reference HT calibrations during GLOBE to laboratory VM calibrations. Equation (11) summarizes the steps implemented for the GLOBE dataset:

$$\eta_{HT,F,SA}\frac{\eta_{HT,L,SA}}{\eta_{HT,F,SA}}\frac{\eta_{HT,L,DSP}}{\eta_{HT,L,SA}}\frac{\eta_{VM,L,DSP}}{\eta_{HT,L,DSP}}=\eta_{VM,L,DSP}. \quad (11)$$

The procedure accounts for target type (HT or VM), measurement methodology (i.e., only at focus F or over the focal volume at different ranges L), and signal analyzer (SA, DSP, SAW).[20]

The calibration process is based on the theoretical relationship[18,21] among SNR, η, and HT reflectance ρ^*,

$$\mathrm{SNR}_{HT}(L)=\frac{\eta P_T \pi R^2 \rho^*}{Bh\nu L^2\left[1+\left(\frac{\pi R^2}{\lambda L}\right)^2\left(1-\frac{L}{F}\right)^2\right]}, \quad (12)$$

where L is the distance from the telescope primary mirror. For measurements at focus, $L = F$, Eq. (12) reduces to

$$\mathrm{SNR}_{HT}(F)=\frac{\eta P_T \pi R^2 \rho^*}{Bh\nu F^2}. \quad (13)$$

The radiometric standard HT used during the GLOBE deployment was a 0.2-m-diameter disk covered with 120-grit silicon carbide sandpaper with known reflectance ρ^*, spinning at ~1710 r.p.m. at a ~45° angle to the lidar beam axis. Reflectance at the two lidar wavelengths was determined[22] to be $\rho^*(9.1\ \mu m) = 5.08 \times 10^{-3}\ sr^{-1}$ and $\rho^*(10.6\ \mu m) = 9.76 \times 10^{-3}\ sr^{-1}$.

For each data system used in GLOBE, η_{HT} can be obtained by comparison of measured SNR_{HT} with theoretical SNR_{HT} from Eq. (12) or (13). Equation (12) is used for SNR_{HT} measurements at multiple ranges along the lidar beam axis, within a ~4-m range interval centered on focus. This accounts for ~99% of the integrated signal from a distributed target. The best chi-square statistical fit between measured and theoretical SNR_{HT} from Eq. (12) leads to a value of $\eta_{HT,L}$ that characterizes lidar system performance. This procedure is referred to as range analysis. Values of $\eta_{HT,F}$ or $\eta_{HT,L}$ are subsequently used to determine the lidar calibration factor K in Eq. (10).

When the HT method is used, the extremely strong return signals saturate the second amplifier in the dual-stage amplification detector circuit. This difficulty is circumvented by removal of one of the amplifiers during HT calibration. System noise, however, can be accurately quantified only by the use of both amplifiers. SNR_{HT} is then determined by correction of the measured signal with a gain factor of 28.4 dB, compensating for removal of the second amplifier. HT measurements with the DSP require an additional 20-dB attenuation for the signal to be maintained within the dynamic range of the DSP. These factors are taken into account when SNR_{DSP} and SNR_{SAW} are calculated.

The calibration procedure begins with estimates of lidar system efficiency $\eta_{HT,F,SA}$ during GLOBE, obtained with the SA from the HT placed at lidar focus. Calibration measurements were not available at any other range during deployment, because of the practical difficulty of aligning the HT on focus from a scissor lift platform ~5 m above ground level at a distance of ~10 or ~50 m from the aircraft.

Although calibration at focus is adequate under restricted conditions, range analysis provides a more detailed mapping of the entire lidar range response, which can be compared with lidar theory for a more comprehensive system performance assessment. Range analysis can be implemented much more easily in the laboratory for CW lidars operated at relatively short focal distances. Estimates of $\eta_{HT,L,SA}$ inferred from a full range analysis in the laboratory were therefore compared with nearly simultaneous measurements of $\eta_{HT,F,SA}$ for ~10-m focus. The two methods yield values of η_{HT} that agree to within a few percent, i.e., $\eta_{HT,L,SA}/\eta_{HT,F,SA} \cong 1$. These results validate the field calibration approach at focus and provide the first transfer function term in Eq. (11). Similar results are expected for the longer focal range, 50 m, used during GLOBE II. However,

equipment was not available to conduct an accurate range analysis at this focal distance in the laboratory.

DSP was not used for GLOBE calibration, as its gain setting was optimized for aerosol measurements; consequently the DSP was saturated by strong HT signals. Following GLOBE II, however, modifications were made to the DSP system to allow gain selection to match measurement conditions. Because the DSP and SAW were the preferred data systems for aerosol measurements, appropriate conversions must be derived from HT measurements with the SA. Laboratory intercomparisons were made subsequent to GLOBE to obtain transfer functions among lidar efficiencies $\eta_{HT,L,DSP}$, $\eta_{HT,L,SAW}$, and $\eta_{HT,L,SA}$. After the characteristic nonlinear response of the SAW was taken into account, $\eta_{HT,L,DSP}$ and $\eta_{HT,L,SAW}$ were in agreement, indicating that the same transfer function could be used for SAW and DSP. Results showed that $\eta_{HT,L,DSP}/\eta_{HT,L,SA} \cong \eta_{HT,L,SAW}/\eta_{HT,L,SA} \sim 1.3$, providing the second transfer function term in Eq. (11). The transfer function differs from unity because the SA underestimates the HT SNR throughout the range analysis by ~1 dB when compared with DSP. This is most likely the result of truncation of the HT return signal by the limited SA bandwidth (0.36 MHz), because the discrepancy is more pronounced in range analysis when the return signal frequency distribution is broadened as the lidar beam cross section on the HT increases away from focus.

In the final step of the calibration procedure, near-simultaneous range analysis measurements are conducted for the standard HT and for well-characterized, artificially generated aerosols. The calibration aerosols consist of spherical silicone oil droplets with diameters ranging from ~1 to 20 μm, with complex indices of refraction m(9.1 μm) = 1.16 + i0.59 and m(10.6 μm) = 1.5 + i0.0174.[19] This resulted in a lidar efficiency $\eta_{VM,L,DSP}$ that was more representative of lidar response to atmospheric targets and that was consistently lower than $\eta_{HT,L,DSP}$ by a factor of ~1.8 (Fig. 3). To our knowledge, this kind of discrepancy has not been previously reported in the literature. Checks of internal consistency of the data do not indicate lidar system anomalies or erroneous signal analysis methodology that could explain the discrepancy (see Section 8). These results emphasize the desirability of using a calibration target that closely resembles the scattering properties of the atmospheric target. The $\eta_{VM,L,DSP}/\eta_{HT,L,DSP}$ ratio of 0.56, from the last step, combined with the other conversion factors in Eq. (11), results in an overall conversion factor of $\eta_{VM,L,DSP} = 0.73\ \eta_{HT,F,SA}$.

Total lidar system efficiency η implicitly depends on P_T, because a change in P_T may imply a change in laser beam quality. Changes may reflect slight misalignment and degradation in heterodyne mixing of backscattered and LO beams that would affect coherent detection. It is difficult to predict this

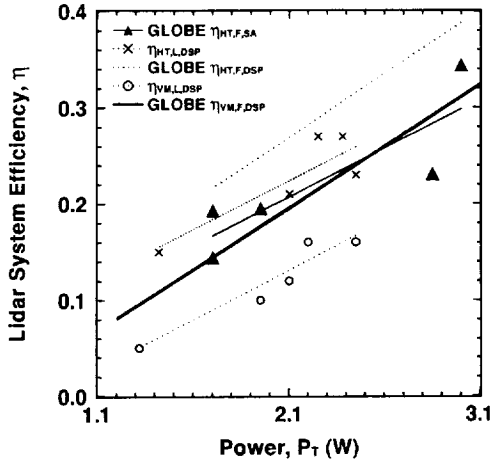

Fig. 3. Total system efficiency η as a function of average laser output power for the 9.1-μm CW Doppler lidar using both HT and well-characterized, artificially generated aerosols.

effect by means of modeling system performance, or to estimate it by measurement of heterodyne efficiency. Instead, detailed power-dependent measurements were made to document efficiency dependence on P_T, both in GLOBE and subsequently in the laboratory with similar operating conditions. During GLOBE II calibrations, for example, P_T(9.1 μm) dropped from ~3.0 to 1.7 W: pre-GLOBE (3.0 and 2.85 W), mid-GLOBE ~1 month later (1.95 W), and post-GLOBE calibration ~2 weeks later (1.70 W). Therefore a similar range of power was investigated in the laboratory with the HT and VM methods. Results are shown in Fig. 3. Although the data exhibit some scatter, a consistent decrease of efficiency with decreasing P_T was found with both methods. A linear least-squares fit was used to estimate $\eta_{HT,F,SA}$, $\eta_{HT,L,DSP}$, and $\eta_{VM,L,DSP}$ as functions of P_T. This relationship was then combined with Eq. (11) to obtain $\eta_{VM,F,DSP}$ as a function of P_T, which was then used to estimate total system efficiency for various lidar power levels during individual GLOBE flights. This represents the completion of the final step in the calibration procedure. At power levels above those of Fig. 3, lidar system efficiencies for VM and HT asymptotically approach ~0.20 and ~0.35, respectively.[19] With Eq. (10), each corrected efficiency $\eta_{VM,F,DSP}$, was converted to K and used in Eq. (9) to obtain β from SNR measurements. Values for K varied over the range 2.7×10^{-15}–2.2×10^{-14} J m^{-1} sr^{-1} for the 9.1-μm lidar. However, for the 10.6-μm lidar with $\eta_{VM,F,DSP} \sim 0.012$, η and K were virtually independent of P_T; any apparent trends lay within the scatter of experimental measurements of HT and VM. Hence a constant $K \cong 3.8 \times 10^{-14}$ J m^{-1} sr^{-1} was used. Power-dependent estimates of efficiency account for laser degradation or slight misalignment affecting the final calibration factor. This approach ensures more accurate conversion of SNR to backscatter, especially under field conditions in which beam-quality assessment and optical realignment are not always possible.

The power-dependent, total system efficiency of the 9.1-μm lidar was investigated. Measurements with a Spiricon beam profiler indicated the beam shape is Gaussian and is unaffected by changes in P_T. No evidence of higher-order, off-axis vibrational modes was found at higher frequencies. However, laboratory measurements indicated that below 3 W, laser output power provides insufficient LO power to permit shot-noise-limited operation of the receiver. Previous calibration studies[23] have incorporated a shot-noise correction factor α into the lidar SNR equation. In the present formulation, the shot-noise correction factor as well as the effects of other system nonidealities are taken into account implicitly by the total system efficiency term η. No attempt has been made here to derive α explicitly because shot noise was not measured during GLOBE. Shot-noise variation is related to variation in laser output power P_T, which was measured frequently. Thus it is important for GLOBE calibration to characterize changes in η as a function of P_T. In our methodology the calibration factor K, inversely proportional to η, takes into account the effect of varying shot noise before conversion of the SNR to β, Eq. (9). It is important to note that as a consequence of our calibration methodology, η may vary, in contrast to previous studies in which it was assumed that η is constant, e.g., Refs. 15 and 23.

Similarly the low system efficiency of the 10.6-μm lidar was investigated. Again, measurements indicated a Gaussian beam shape unaffected by changes in P_T, with no evidence of off-axis vibrational modes. Photon-generated shot noise of the LO detector current dominated all other system noise. The low 10.6-μm system efficiency is attributed primarily to degraded optical efficiency, particularly degradation of the quarter-wave plate that converts between circular and linear polarization. Internal consistency checks show no evidence of in-flight or flight-to-flight variability that could be traced to the quarter-wave plate. The SNR estimated for GLOBE flights with Eq. (3) was verified to be independent of G, despite ~5 orders of magnitude variation in backscatter.[24] Despite low efficiency, the 10.6-μm system obtained valid backscatter measurements above the sensitivity, independent of system fluctuations.

Uncertainty in absolute backscatter estimation has been derived from (1) the root sum of squares (rss) of random errors for each of the measurable lidar parameters in Eqs. (10) and (12), as determined from observed variation during calibration measurements described earlier; (2) the DSP SNR estimation algorithm, using SNR calculations with simulated signals attenuated in stepwise fashion and integrated for 5 s (Section 5); and (3) Eq. (9) which combines the uncertainties in (1) and (2). Two cases are considered: SNR well above detection threshold (SNR $\gg$ $SNR_{THRESHOLD}$) and SNR near threshold (SNR $\cong$ $SNR_{THRESHOLD}$; see Section 8 and Table 3). Table 2 summarizes uncertainties for both lidar systems related to calibration, signal estimation, and backscatter estimation. The results show that when one is estimating β for strong signals, calibration uncertainty dominates over SNR uncertainty, whereas the opposite holds under marginal SNR conditions. Uncertainty in SNR estimation for the SAW algorithm is smaller than for the DSP by a factor of $\sim(11{,}500/65{,}536)^{0.5} \cong 0.4$, based on 1-s and 5-s integrations for the SAW and DSP, respectively, during periods when the SAW noise floor was well behaved.

Table 2. Lidar Parameter, Signal, and Backscatter Estimation Uncertainties[a]

Term in Eqs. (9), (10), (12)		1-σ Uncertainty (Percent)
B		1
f		1
R		2
P		3
SNR		11
ρ^*		14
Conversion of η_{HT} to η_{VM}		10
η		21 (rss)[b]
K		21 (rss)
	Strong Signal	Marginal Signal
SNR(DSP)	5	33
SNR(SAW)	2	14
β(DSP)	22 (rss)	39 (rss)
β(SAW)	21 (rss)	25 (rss)

[a]Analysis of uncertainties contributing to atmospheric absolute backscatter estimation for high SNR (SNR $\gg$ $SNR_{THRESHOLD}$) and low SNR (SNR $\cong$ $SNR_{THRESHOLD}$; see Table 3).
[b]Root sum of squares.

7. Examples of Aerosol Backscatter Estimates

As an illustration of the degree of comparison among data systems and between CW lidars, this section presents examples of backscatter estimates obtained from GLOBE II, flight 13, 3 June 1990, over the Pacific Ocean to the southeast of Japan. A series of level flights at different altitudes was made over a common region. Figure 4(a) compares time series of $\beta(\pi, 10.6\ \mu m)$ from SA and DSP signal analyzers, with altitude superimposed. Figure 4(b) is a scatter-

Table 3. Lidar System SNR and Backscatter Sensitivity ($\times m^{-1}\ sr^{-1}$) as a Function of Signal Analyzer Type and Wavelength[a]

	9.1 μm				10.6 μm			
	Theory		Measurement		Theory		Measurement	
Signal Analyzer	SNR	β	SNR	β	SNR	β	SNR	β
SA	–	–	0.05	34	–	–	0.09	170
DSP	0.019	5.2	0.020	5.4	0.019	14	0.027	20
SAW	0.008	2.8	0.010	3.5	0.008	7.5	0.010	9.3

[a]Theoretical predictions are based on ensemble statistics for Gaussian distribution, compared with sensitivity from signal-processing algorithms applied to GLOBE aerosol backscatter measurements. Details of the calculations are described in the text.

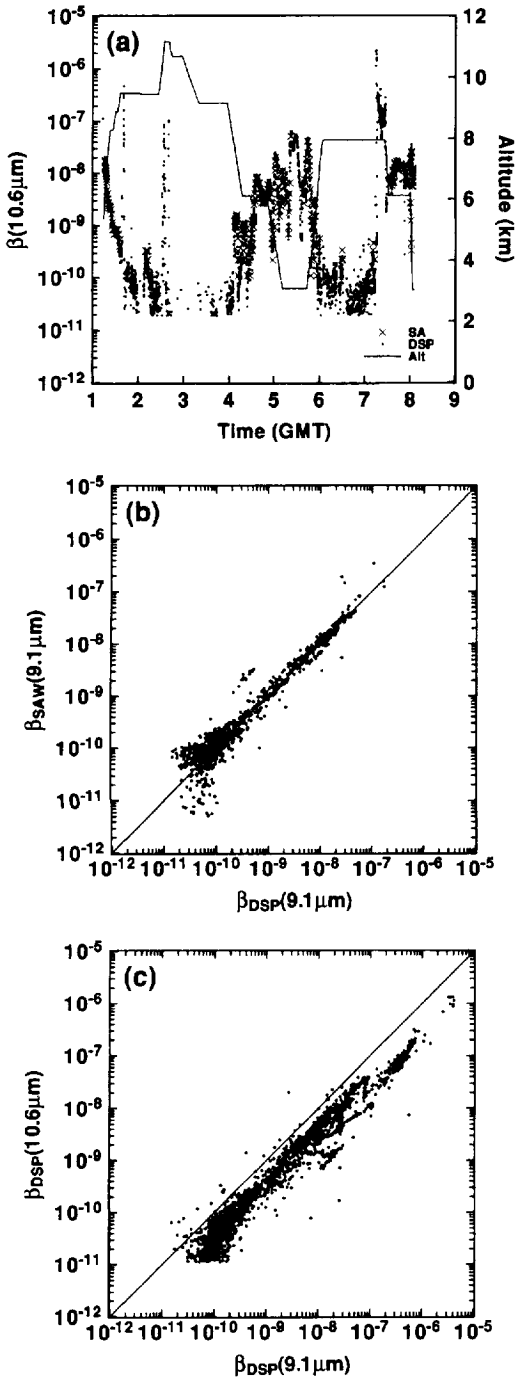

Fig. 4. Intercomparisons of the aerosol backscatter coefficient $\beta(\pi)$ (in $m^{-1}\ sr^{-1}$) at 9.1 and 10.6 μm, as estimated from SA, SAW, and DSP signal analyzer measurements during GLOBE II, flight 13, 3 June 1990, over the remote northwestern Pacific Ocean: (a) time series of $\beta(\pi, 10.6\ \mu m)$ from SA and DSP, with altitude (alt) superimposed, (b) scatterplot of $\beta(\pi, 9.1\ \mu m)$ estimates from DSP and SAW, (c) scatterplot of $\beta(\pi, 9.1\ \mu m)$ and $\beta(\pi, 10.6\ \mu m)$ from DSP. DSP and SAW estimates are based on 11,500 (5-s) and 65,536 (1-s) integrations, respectively.

plot comparing $\beta(\pi, 9.1\ \mu m)$ from SAW and DSP signal analyzers. Scatter increases with decreasing backscatter in part because of the difference in sample time (1 versus 5 s), hence in effective sample volume. Figure 4(c) is a scatterplot comparing $\beta(\pi, 9.1\ \mu m)$ with $\beta(\pi, 10.6\ \mu m)$ from the DSP. Backscatter estimates from the three signal analyzers were found to agree to within a factor of 2 or better at each wavelength over the entire GLOBE measurement set, except for increasing scatter near the respective detection thresholds. These results provide a foundation for geophysical analysis and interpretation of the GLOBE CW lidar measurements and their relationship to aerosol data from other collocated sensors, described elsewhere.[24,25]

The uncertainty estimates in Table 2 represent only instrumental contributions to the backscatter measurement uncertainty, determined by the use of well-defined synthetic signals in the laboratory. However, near-simultaneous comparative measurements with the SAW and DSP show considerably more scatter for atmospheric backscatter signals than for the synthetic signals. This additional scatter is particularly apparent in low backscatter conditions. It is still present, although much weaker, in high-backscatter, high-SNR conditions. The additional scatter must, therefore, be introduced by atmospheric factors, rather than instrumental problems. We tentatively attribute the increased scatter to inadequate atmospheric sampling statistics for low concentrations of the micrometer-sized particles that usually dominate aerosol backscatter at the 9.1- and 10.6-μm wavelengths. If particle counts (N) follow Poisson statistics (as expected for uniform particle concentrations), then the relative counting standard deviation for these particles should be roughly $N^{-1/2}$. The corresponding relative scatter in backscatter estimates should therefore be $\sim(2/N)^{1/2}$ for two independent signal processors that are both sampling the same uniform backscatter field. This scatter can be quite large for low-backscatter conditions near the detection thresholds of the CW lidars. Under these conditions, micrometer-sized scatterers are sometimes completely missing from the lidar sample volume, and the remaining backscatter is provided by higher concentrations of weakly scattering small particles.

8. Conclusions

A key objective of the GLOBE program was to characterize aerosol properties in the relatively clean remote middle and upper troposphere. This challenging task required a detailed characterization of the lidar system performance, careful attention to calibration procedures, and development of new signal-processing methods. These procedures ensured that in-flight measurements of aerosol backscatter could be rigorously traced to absolute radiometric calibrations and that atmospheric variability could be separated from any instrumental effects. The calibration methodology on which our absolute backscatter estimates are based was chosen to facilitate the calibration and monitoring of CW lidar performance under less-than-ideal field conditions. Our approach varies from that of previous studies, which have sought to characterize the lidar system

at the earliest stage possible, for example, LO levels and optical component performance.

Occasionally during GLOBE, backscatter was observed to drop below the detection threshold of all three signal analyzers ("dropout"). Weak signal conditions were simulated in the laboratory during characterization of the signal analyzers. In both cases, the SAW exhibited the best sensitivity because of high throughput. Attempts to improve the detection threshold of the DSP have met with some success when additional integration was used during postprocessing; the practical limit of integration is ~5 s, or ~11,500 spectra. Further integration provides no additional benefit because of the cumulative effect of airspeed errors on estimation of signal peak position during integration or the smearing of signals as a result of small but steady changes in airspeed. Table 3 summarizes the minimum SNR and backscatter sensitivity for combinations of signal analyzer and lidar system based on theory and observation. Theoretical estimates were obtained by assuming that short-term noise fluctuations in the SAW and DSP conform to ensemble statistics for a Gaussian distribution. Thus it was assumed that $\mathrm{SNR} \cong 2\sigma/\mu = 2/N^2$, where the factor of 2 arises from the single-channel SNR evaluation criterion defined in Section 4. N was set equal to 11,500 and 65,536 integrations for the DSP and the SAW, respectively. Theoretical estimates are not included for the SA, which was operated in analog mode. For GLOBE II, the time-weighted values for P_T and K were calculated to be 2.2 W and 4.2×10^{-15} J m^{-1} sr^{-1}, respectively, for the 9.1-μm lidar and 7.4 W and 3.8×10^{-14} J m^{-1} sr^{-1}, respectively, for the 10.6-μm lidar. Empirical backscatter sensitivity was inferred from distributions of backscatter versus speed difference (not shown) for GLOBE flights in which dropouts occurred.[17] The generally excellent agreement between theory and measurement in Table 3 indicates that short-term random fluctuations in the SAW and DSP data systems conform to a chi-square distribution for an ensemble average. Furthermore, the factor of 2 used in the single-channel SNR evaluation criterion (Section 4) is successful in maintaining a low false alarm rate during signal processing. The discrepancy between theory and measurement for the combination of DSP signal analyzer and 10.6-μm lidar is attributed to fluctuating power output of the 10.6-μm lidar as noted in Section 6.

Atmospheric aerosol backscatter estimates from the GLOBE survey mission measurements with 9.1- and 10.6-μm CW focused Doppler lidars have been obtained by the use of innovative procedures and algorithms described above. The first backscatter measurements at 9.1 μm were made during GLOBE, as well as the first backscatter intercomparisons between 9.1- and 10.6-μm lidars. For GLOBE II, a signal analyzer based on relatively recent DSP technology was added. Absolute backscatter estimates have been based on rigorous calibration procedures that use both a HT with known reflectance and a new method that uses aerosols with known physical and optical properties generated under laboratory conditions. Calibration involved measurements not only at focus, but also throughout the lidar sample volume. Lidar system efficiency, as defined in this paper, was determined as a function of laser output power; this innovative approach simplifies implementation in the field while taking into account all system nonidealities. It was found that HT calibration leads to a system efficiency that is a factor of ~1.8 larger than for calibration based on aerosols. Various checks of the data have failed to reveal internal inconsistencies that would explain the difference. We suggest, therefore, that this result arises from dissimilarity in the fluctuations and statistical properties of light scattered from HT's compared with diffuse aerosols.[26] Within the context of the wide variation in atmospheric scatterers, however, this discrepancy is rather minor compared with tropospheric backscatter in optically clear air, which may vary over several orders of magnitude. Nevertheless this result is potentially useful to reconcile theoretical predictions of lidar performance with calibration measurements, as well as for more precise assessments of the performance of ground-based, airborne, and satellite-borne coherent Doppler lidar systems.

SNR and backscatter estimates from the three signal analyzers have been found to agree to within a factor of 2 or better. Both CW lidars provide sensitive, high temporal and spatial resolution measurements of aerosol backscatter. When operated simultaneously with juxtaposed sampling volumes, the combined lidars are capable of supporting limited measurements of spectral dependence of the scatterers, which allow inferences of chemical composition to be made.[24]

The authors gratefully acknowledge support under NASA contract NAS8-37814 awarded to Sverdrup Technology, Inc., Huntsville, Ala., NASA Cooperative Agreement NCC8-22 with the Institute for Global Change Research and Education (IGCRE), and NASA contract NAS8-38775 (recently concluded) and NASA Sub-contract 93-216 awarded to the Universities Space Research Association (USRA), Huntsville, Ala. IGCRE is jointly operated by the University of Alabama in Huntsville and USRA. The authors gratefully acknowledge valuable suggestions from Rod Frehlich, University of Colorado. Laboratory measurements were conducted at the Aerosol Optical Properties Laboratory at the NASA Marshall Space Flight Center. The authors gratefully acknowledge the assistance of the staff of the NASA Ames Research Center, which managed ground and air operation of the NASA DC-8 aircraft during the GLOBE survey mission. Finally, the authors gratefully acknowledge the support of Ramesh Kakar, Office of Mission to Planet Earth, NASA Headquarters.

References and Notes

1. J. Rothermel, D. A. Bowdle, J. M. Vaughan, and M. J. Post, "Evidence of a tropospheric aerosol backscatter background mode," Appl. Opt. **28,** 1040–1042 (1989).
2. D. A. Bowdle, J. Rothermel, J. M. Vaughan, and M. J. Post, "Aerosol backscatter measurements at 10.6 micrometers with airborne and ground-based CO_2 Doppler lidars over the Colorado high plains 2. Backscatter structure," J. Geophys. Res. **96,** 5337–5344 (1991).
3. J. M. Vaughan, D. W. Brown, C. Nash, S. B. Alejandro, and G. G. Koenig, "Atlantic atmospheric aerosol studies. 2. Compendium of airborne backscatter measurements at 10.6 μm," J. Geophys. Res. **100,** 1043–1065 (1995).
4. R. L. Schwiesow, R. E. Cupp, V. E. Derr, E. W. Barrett, R. F. Pueschel, and P. C. Sinclair, "Aerosol backscatter coefficient profiles measured at 10.6 μm," J. Appl. Meteorol. **20,** 184–194 (1981).
5. W. D. Jones, J. W. Bilbro, S. C. Johnson, H. B. Jeffreys, L. Z. Kennedy, R. W. Lee, and C. A. DiMarzio, "Design and calibration of a coherent lidar for measurement of atmospheric backscatter," in *The Human in the Photo-Optical System* (New York), R. L. Minter, ed., Proc. Soc. Photo-Opt. Instrum. Eng. **5,** 66–71 (1982).
6. W. D. Jones, L. Z. Kennedy, and R. W. Lee, "Determination of atmospheric backscatter at 10.6 μm," in *Coherent Infrared Radar Systems and Applications II,* R. C. Harney, ed., Soc. Photo-Opt. Instrum. Eng. **415,** 77–84 (1983).
7. W. D. Jones, L. Z. Kennedy, J. W. Bilbro, and H. B. Jeffreys, "Coherent focal volume mapping of a continuous-wave CO_2 Doppler lidar," Appl. Opt. **23,** 730–733 (1984).
8. J. W. Bilbro, C. A. DiMarzio, D. E. Fitzjarrald, S. C. Johnson, and W. D. Jones, "Airborne Doppler lidar measurements," Appl. Opt. **25,** 3952–3960 (1986).
9. J. L. Gras and W. D. Jones, "Australian aerosol backscatter survey," Appl. Opt. **28,** 852–856 (1989).
10. W. E. Baker, G. D. Emmitt, P. Robertson, R. M. Atlas, J. E. Molinari, D. A. Bowdle, J. Paegle, R. M. Hardesty, R. T. Menzies, T. N. Krishnamurti, R. A. Brown, M. J. Post, J. R. Anderson, A. C. Lorenc, T. L. Miller, and J. McElroy, "Lidar measured winds from space: a key component for weather and climate prediction," Bull. Am. Meteorol. Soc. **76,** 869–888 (1995).
11. D. A. Bowdle, J. Rothermel, J. E. Arnold, and S. F. Williams, "The GLObal backscatter experiment Pacific survey mission: results and implications for LAWS," in *Coherent Laser Radar: Technology and Applications,* Vol. 12 of 1991 OSA Technical Digest Series (Optical Society of America, Washington, D.C., 1991), pp. 290–292.
12. The mention of brand names in this paper is for information purposes only and does not constitute an endorsement of the product by the authors, their institutions, or sponsors.
13. J. Rothermel, D. A. Bowdle, J. M. Vaughan, D. W. Brown, and A. A. Woodfield, "Calculation of aerosol backscatter from airborne continuous-wave focused CO_2 Doppler lidar measurements 1. Algorithm description," J. Geophys. Res. **96,** 5293–5298 (1991).
14. J. H. Shapiro, "Precise comparison of experimental and theoretical SNRs in CO_2 laser heterodyne systems: comments," Appl. Opt. **24,** 1245–1247 (1985).
15. J. M. Vaughan, R. D. Callan, D. A. Bowdle, and J. Rothermel, "Spectral analysis, digital integration and measurement of low backscatter in coherent laser radar," Appl. Opt. **28,** 3008–3014 (1989).
16. M. I. Skolnik, *Introduction to Radar Systems* (McGraw-Hill, New York, 1962).
17. J. Rothermel, D. A. Bowdle, and J. M. Vaughan, "Calculation of aerosol backscatter from airborne continuous-wave focused CO_2 Doppler lidar measurements 2. Algorithm performance," J. Geophys. Res. **96,** 5299–5305 (1991).
18. C. M. Sonnenschein and F. A. Horrigan, "Signal-to-noise relationships for coaxial systems that heterodyne backscatter from the atmosphere," Appl. Opt. **10,** 1600–1604 (1971).
19. M. A. Jarzembski, V. Srivastava, and D. M. Chambers, "Lidar calibration technique using laboratory-generated aerosols," Appl. Opt. **35,** 2096–2108 (1995).
20. Hereafter, with obvious exceptions, total lidar system efficiency η is referenced to the type of target (HT, SPM, or VM), measurement coverage (at focus F or over the focal volume at different ranges L), and signal analyzer (DSP, SA, or SAW).
21. M. J. Kavaya, S. W. Henderson, and R. G. Frehlich, "Theory of CW lidar aerosol backscatter measurements and development of a 2.1 μm solid-state pulsed laser radar for aerosol backscatter profiling," NASA Contr. Rep. CR-4347 (NASA, Washington, D.C., 1991).
22. M. J. Kavaya, "The JPL lidar target calibration facility," in *Third Topical Meeting on Coherent Laser Radar: Technology and Applications* (Optical Society of America, Washington, D.C., 1985), p. II.1.
23. M. J. Post and R. E. Cupp, "Optimizing a pulsed Doppler lidar," Appl. Opt. **29,** 4145–4158 (1990).
24. V. Srivastava, D. A. Bowdle, M. A. Jarzembski, J. Rothermel, D. M. Chambers, and D. R. Cutten, "High-resolution remote sensing of sulfate aerosols from CO_2 lidar backscatter," Geophys. Res. Lett. **22,** 2373–2376 (1995).
25. D. R. Cutten, R. F. Pueschel, D. A. Bowdle, V. Srivastava, A. D. Clarke, J. Rothermel, J. D. Spinhirne, and R. T. Menzies, "Multi-wavelength comparison of modeled and measured remote tropospheric backscatter over the Pacific Ocean," J. Geophys. Res. (to be published).
26. M. Harris, G. N. Pearson, C. A. Hill, and J. M. Vaughan, "The fractal character of Gaussian–Lorentzian light," Opt. Commun. **116,** 15–19 (1995).